

Fragile Insulator and Electronic Nematicity in a Graphene Moiré System

Lei Chen[†], Haoyu Hu[†], Qimiao Si

Department of Physics and Astronomy & Rice Center for Quantum Materials, Rice University,
Houston, Texas 77005, USA

Graphene heterostructures can host narrow moiré electron bands¹, in which the effect of correlations is amplified and a rich variety of electronic properties develop. An insulating state is a prominent feature in these systems, and may hold the key to understanding the correlation effect. Here we advance the notion of a fragile insulator, a correlation-driven insulating state that is on the verge of a delocalization transition into a bad metal. Using a realistic multiorbital Hubbard model as a prototype for narrow band moiré systems, we realize such a fragile insulator and demonstrate a nematic order in this state as well as in the nearby bad metal regime. Our results are consistent with the observed electronic anisotropy in the graphene moiré systems^{2–6} and provide a natural understanding about what happens when the insulator is tuned into a bad metal^{7–9}. We propose the fragile insulator and the accompanying bad metal as competing states at integer fillings that analogously anchor the overall phase diagram of these and related moiré systems.

[†]L.C. and H. H. contributed equally to this work.

The field of correlated moiré systems is highlighted by the emergence of superconductivity and correlated insulators in the twisted bilayer graphene (TBG) at magic angles^{10–13}, trilayer graphene heterostructures with hexagonal boron nitride (TLG/hBN)^{14,15} and related structures. The effect of electron correlations is amplified by the narrowness of the moiré bands at the magic angles¹. The insulators appear at the partial but integer fillings of the moiré bands, while superconductivity develops when the charge carrier concentration is tuned away from such fillings.

The insulator is believed to be key to elucidating the correlation physics of the moiré systems^{16–21}. However, understanding its nature remains a pressing open question. Here we address the issue, departing from several motivating factors. One type of considerations concern the insulating nature *per se*. The insulating behavior develops at energy scales that can be very low compared to either the effective Coulomb repulsion U or the width W of the moiré bands. For instance, for the magic-angle TBG devices, the electrical resistivity shows an insulating-like temperature dependence below about 4 K (Refs. 10,11), which is more than one decade lower than the scale $U \sim W \sim 10$ meV. Moreover, recent experiments have shown that the insulator can be tuned away quantum mechanically: This happens by varying the strength of the electron correlations without changing the carrier concentration while the superconductivity persists, raising the question about whether the insulator anchors the phase diagram at all^{7–9}.

We are also motivated by the consideration of electronic orders, a rich landscape of which is one of the salient characteristics of strongly correlated systems^{22,23}. Recently, measurements by scanning tunneling microscopy (STM)^{2–5} have revealed evidence for electronic nematic correlation in the normal state (above the superconducting transition temperature) of the magic-angle TBG. The local density of states shows a three-fold anisotropy², implying a large nematic susceptibility and possibly even a nematic order. Importantly, the effect maximizes near the insulating phase of the half-filled moiré bands (*i.e.*, two electrons or holes per unit cell of the moiré superlattice). These STM observations are complemented by transport measurements⁶, which furthermore connect the nematic correlation with superconductivity. Understanding the nematic correlation is important, as it is primed for clues about the underlying correlation physics.

We choose to focus on the TLG/hBN system as a prototype case where the correlation physics can be isolated and non-perturbative theoretical analyses are possible. In this system, the moiré superstructure (Fig. 1a) results from a small difference between the in-plane lattice constants of the ABC stacked TLG (see Supplementary Information, Fig. S1) and hBN^{14,15,24,25}. In the case of the magic-angle TBG, a topological obstruction to the construction of Wannier orbitals for their

moiré bands has been actively discussed (for example, Refs. 26,27). The TLG/hBN structure under a particular direction of the perpendicular voltage bias, while having electronic properties with considerable similarities to those of the magic-angle TBG, do not have this obstruction^{14,15}. Consequently, their moiré bands are faithfully represented by a two-orbital Hubbard Hamiltonian²⁵, comprising the kinetic part, H_0 , and the interaction part $H_U + H_V$ (see Methods). Importantly, here we can investigate the regime of prime interest, *viz* with intermediate correlations, $U/W \sim 1$, using non-perturbative methods. Our primary tool will be the recently developed Variational Monte Carlo (VMC) method that incorporates the correlation effects of not only the Hubbard interaction but also the Hund's coupling²⁸.

We consider the half-filling case ($\nu = 2$, corresponding to 1 electron per valley per moiré unit cell), keeping in mind the aforementioned motivations. To be definite, we focus on the case with a perpendicular voltage bias, which fixes the tight-binding parameters (see Fig. 1b, Methods and Supplementary Information) for H_0 , and allows for an estimate of the parameters for H_U (the onsite Hubbard interaction U and Hund's coupling J_H) and those for H_V (the density-density interaction V and spin-valley exchange interaction V_H between nearest-neighbor sites)²⁵. A metal-insulator transition (MIT) could arise in the multiorbital model, in spite of having an even number of electrons per unit cell, due to the onsite interactions. We address their effects by performing a saddle-point analysis within a U(1) slave-spin method (see Methods)²⁹. Focusing on the paramagnetic phase that preserves the time reversal and translation symmetries, the quasiparticle weight is the same for the two valleys, $Z_+ = Z_- = Z$. The results for Z vs. U/W , for various values of the ratio J_H/U , are shown in Fig. 1c. In the absence of the Hund's coupling, $J_H = 0$, a metal-to-insulator transition occurs at $U_c(J_H = 0)/W \approx 1.65$. As Fig. 1c also shows, even a relatively small Hund's coupling considerably enhances the localization effect, and turns the threshold for the metal-insulator transition to about $U_c/W \approx 1$.

The metallic regime in proximity of the metal-to-insulator transition corresponds to a bad metal, where the quasiparticle weight Z has been much reduced from the free-electron value 1 (Refs. 23,30). Likewise, we dub the insulating phase in proximity of the insulator-to-metal transition to be a fragile insulator. Here, the insulating gap is considerably smaller than either U and W . Correspondingly, the temperature scale for the onset of the insulating behavior is expected to be small compared to U/k_B and W/k_B ; this is precisely the behavior observed in the graphene moiré systems^{10,11}. We expect such behavior to occur in other integer fillings between charge neutrality and fully filled moiré bands, *albeit* with a different threshold interaction for the transition. For

instance, a similar transition from bad metal to fragile insulator occurs in the quarter-filling case ($\nu = 1$), as is also shown in Fig. 1c.

We next analyse the possible electronic orders, including nematicity. The effect of onsite interactions is studied using the non-perturbative VMC method, that incorporates the correlation effect of the Hund's coupling²⁸ (see Methods). In the intermediate correlation regime, we find that the ground state has a collinear antiferromagnetic (CAFM) order (Fig. 2a), with the pitch wavevector located at $\mathbf{Q} = \mathbf{M} = (0, \frac{2\sqrt{3}}{3}\pi)$ of the moiré Brillouin zone (BZ) [or equivalently $(\pi, \frac{\sqrt{3}}{3}\pi)$ and $(-\pi, \frac{\sqrt{3}}{3}\pi)$]. Fig. 2c shows that its energy is lower than that of not only the paramagnetic phase (*i.e.*, without any order) but also the competing uniaxial antiferrovalley (UAFV) order (Fig. 2b). To identify the strength of the magnetic order, we calculate the spin structure factor defined as

$$S(\mathbf{Q}) = \frac{1}{N} \sum_{i,j} \langle \mathbf{S}_i \cdot \mathbf{S}_j \rangle e^{i\mathbf{Q} \cdot (\mathbf{R}_i - \mathbf{R}_j)}, \quad (1)$$

at $\mathbf{Q} = \mathbf{M}$, where N is the number of sites in the lattice. We define the magnetic order parameter as $m^2 = S(\mathbf{M})/N$, which is shown as a function of J_H/U for a fixed U/W (Fig. 2d) and *vs.* U/W for a fixed J_H/U (Fig. 2e) as a function of J_H/U . The magnetic order exists both in the fragile insulating and bad metal regimes.

We are now in position to analyse the nematic order. We can classify the nematic order in terms of the breaking of the C_6 symmetry, which is an approximate symmetry of the system and exists in the model Hamiltonian, or the C_3 symmetry, which survives the weak couplings that exist in the system beyond the model^{14,15,24,25}. The irreducible representations of the groups D_6 and D_3 are given in Table I. Of interest to our analysis is the following nematic order parameter (E_2/E representation, depending on the classification scheme):

$$\sigma = \frac{1}{N} \sum_i \left[\langle \mathbf{S}_i \cdot \mathbf{S}_{i+e_1} \rangle + e^{i\frac{2\pi}{3}} \langle \mathbf{S}_i \cdot \mathbf{S}_{i+e_2} \rangle + e^{i\frac{4\pi}{3}} \langle \mathbf{S}_i \cdot \mathbf{S}_{i+e_3} \rangle \right] \quad (2)$$

where $e_{1,2,3}$ labels the nearest-neighbor bonds of the moiré lattice (Fig. 1a). The calculated nematic order parameter σ is shown in Fig. 3a,b, respectively as a function of J_H/U and *vs.* U/W . As a key result of our work, the nematic order parameter is nonzero both in the fragile insulator and bad metal regimes and, moreover, it varies smoothly between these two regimes.

We now assess the stability of this ground state against the intersite interactions, which are significant due to the size of the moiré unit cell. Consider first the nearest-neighbor Hund's exchange coupling. Our VMC calculation finds the CAFM and associated nematic order to be stable for a range of this coupling, up to $V_H^1/W \approx 0.011$ (Fig. 3a). Above V_H^1 , a ferromagnetic order becomes

the ground state. Consider next the effect of the nearest-neighbor Coulomb repulsion V . The CAFM and associated nematic order are stable against the paramagnetic state (without any order) for a range of this coupling, up to $V^1/W \approx 0.31$. It is instructive to note that the VMC approach is non-perturbative and, therefore, advantageous in the intermediate correlation, $U/W \sim 1$, regime of interest here. For comparison, we have carried out a self-consistent Hartree-Fock calculation. We found that the Hartree-Fock method qualitatively captures the transition from CAFM to FM with increasing V_H (see Supplementary Information, Fig. S5a), but misses the V -induced instability of the CAFM state towards the paramagnetic state (Supplementary Information, Fig. S5b). This reflects the underestimation of the correlation effect by the Hartree-Fock method, especially for the paramagnetic state. Nonetheless, the Hartree-Fock calculation suggests that a sufficiently large V makes a charge order viable; its ordering wavevector is \mathbf{K} (Fig. S5b), and hence it is a three-sublattice order and is not expected to be accompanied by a nematic order. We note that, while our purpose is to use the well-defined Hamiltonian as a means to access the qualitative features of the overall phase diagram, for TLG/hBN *per se*, the threshold values we have determined, V_H^1/W and V^1/W , are competitive against the order-of-magnitude estimates for these parameters (which, at $\Delta_V = -20$ meV, are about 0.007 and 0.37, respectively²⁵), suggesting that either a nematic order or an enhanced nematic fluctuation is to be expected for TLG/hBN.

We now turn to the overall implications of our results. First, we have found that whether the parent system is a fragile insulator or a bad metal does not matter much to the nematicity and other electronic orders. This illustrates the insensitivity of the underlying correlation physics to whether the half-filled system happens to be placed on either side of the Mott transition. In other words, regardless of whether the correlated insulator or the bad metal is the ground state at half filling, each can anchor the phase diagram. In both cases, the system is on the verge of electronic delocalization/localization. Indeed, the emerging picture is that the system away from any integer filling can be considered as being anchored by the Mott transition, the electronic localization-delocalization transition at the integer filling that links the fragile insulating and bad metallic regimes. By extension, when the carrier concentration is tuned away from half-filling, the physics in both cases is expected to be similar. This picture, illustrated in Fig. 4, provides a natural understanding for the qualitatively similar electronic behavior, including the emergence of superconductivity, when the system's correlation strength is tuned down and the fragile insulator yields to a bad metal. Thus, the recent observations of Refs. 7–9 are fully compatible with the superconductivity being (primarily) driven by electron-electron interactions.

Second, our work motivates further experiments. So far, experimental studies of the nematic correlation in the graphene moiré systems have focused on the magic-angle TBG. Our analysis suggests that the nematic correlation should also develop in the phase diagram of the TLG/hBN systems, especially near half-filling of their moiré bands. Additionally, it follows from our results that in devices where the insulating phase has turned metallic⁷⁻⁹, nematic correlations will likely persist. Exploring electronic anisotropy, by STM, transport and other means, in those cases will be highly instructive to the understanding of the overall correlation physics of the moiré systems.

Third, Fig. 4 suggests that the physics of the integer-filled moiré systems adiabatically continue when U/W is further enhanced from the fragile insulator/bad metal regime, where U/W is of order unity, to the regime where U/W is larger and the correlated insulator is no longer fragile. The latter is likely the case in the recently realized moiré systems based on the transition-metal dichalcogenides³¹⁻³³. In that regime, a robust Mott insulator at the integer fillings anchors the correlated electron physics at carrier concentrations away from those fillings. The picture advanced here would suggest that the correlation physics in these systems will be adiabatically connected to those in the intermediate correlation regime, although their energy scales, such as the exchange interactions as measured by their kinetic energy, will be smaller.

Finally, by isolating the correlation effect in a model system, our work sets the stage to address how the interplay between the intermediate to strong correlations and bandstructure topology influences the fragile insulator, bad metal and nematicity. The interplay promises to create new phases in the overall phase diagram, but whether and how it will enrich the relationship between the fragile insulator and bad metal on the one hand, and superconductivity on the other, is an exciting open question. Empirically, the continued emergence of new members in the family of correlated moiré systems allows for ascertaining the similarities and differences between these members with differing bandstructure, which will surely illuminate this outstanding issue.

In summary, we have demonstrated an emergent fragile insulator in a graphene moiré system in the physically relevant intermediate correlation regime. This correlated insulator is accompanied by an electronic nematic order, as has been evidenced in the magic-angle twisted bilayer graphene. As such, our work highlights the kind of clues that the nematic correlation provides for the microscopic correlation physics, and motivates its search in related moiré systems. Finally, our work reveals that the same correlation physics is anchored by the parent system at an integer filling of the moiré lattice regardless of whether it is a fragile insulator or a bad metal. This finding offers a natural understanding of a striking puzzle that has emerged from some very recent experiments,

and provides a new perspective about the overall phase diagram of the correlated moiré systems.

1. Bistritzer, R. & MacDonald, A. H. Moiré bands in twisted double-layer graphene. *Proceedings of the National Academy of Sciences* **108**, 12233–12237 (2011).
2. Kerelsky, A. *et al.* Maximized electron interactions at the magic angle in twisted bilayer graphene. *Nature* **572**, 95–100 (2019).
3. Choi, Y. *et al.* Electronic correlations in twisted bilayer graphene near the magic angle. *Nature Physics* **15**, 1174–1180 (2019).
4. Jiang, Y. *et al.* Charge order and broken rotational symmetry in magic-angle twisted bilayer graphene. *Nature* **573**, 91–95 (2019).
5. Xie, Y. *et al.* Spectroscopic signatures of many-body correlations in magic-angle twisted bilayer graphene. *Nature* **572**, 101–105 (2019).
6. Cao, Y. *et al.* Nematicity and competing orders in superconducting magic-angle graphene. *arXiv preprint arXiv:2004.04148* (2020).
7. Saito, Y., Ge, J., Watanabe, K., Taniguchi, T. & Young, A. F. Independent superconductors and correlated insulators in twisted bilayer graphene. *Nat. Phys.* (2020).
8. Stepanov, P. *et al.* The interplay of insulating and superconducting orders in magic-angle graphene bilayers. *arXiv preprint arXiv:1911.09198* (2019).
9. Arora, H. S. *et al.* Superconductivity without insulating states in twisted bilayer graphene stabilized by monolayer wse2. *arXiv preprint arXiv:2002.03003* (2020).
10. Cao, Y. *et al.* Magic-angle graphene superlattices: a new platform for unconventional superconductivity. *Nature* **556**, 43–50 (2018).
11. Cao, Y. *et al.* Correlated insulator behaviour at half-filling in magic-angle graphene superlattices. *Nature* **556**, 80–84 (2018).
12. Lu, X. *et al.* Superconductors, orbital magnets and correlated states in magic-angle bilayer graphene. *Nature* **574**, 653–657 (2019).
13. Yankowitz, M. *et al.* Tuning superconductivity in twisted bilayer graphene. *Science* **363**, 1059–1064 (2019).
14. Chen, G. *et al.* Evidence of a gate-tunable mott insulator in a trilayer graphene moiré superlattice. *Nature Physics* **15**, 237–241 (2019).

15. Chen, G. *et al.* Signatures of tunable superconductivity in a trilayer graphene moiré superlattice. *Nature* **572**, 215–219 (2019).
16. Xu, C. & Balents, L. Topological superconductivity in twisted multilayer graphene. *Phys. Rev. Lett.* **121**, 087001 (2018).
17. Dodaro, J. F., Kivelson, S. A., Schattner, Y., Sun, X. Q. & Wang, C. Phases of a phenomenological model of twisted bilayer graphene. *Phys. Rev. B* **98**, 075154 (2018).
18. Padhi, B., Setty, C. & Phillips, P. W. Doped twisted bilayer graphene near magic angles: Proximity to wigner crystallization, not mott insulation. *Nano letters* **18**, 6175–6180 (2018).
19. Thomson, A., Chatterjee, S., Sachdev, S. & Scheurer, M. S. Triangular antiferromagnetism on the honeycomb lattice of twisted bilayer graphene. *Phys. Rev. B* **98**, 075109 (2018).
20. Xie, M. & MacDonald, A. H. Nature of the correlated insulator states in twisted bilayer graphene. *Phys. Rev. Lett.* **124**, 097601 (2020).
21. Pizarro, J., Calderón, M. & Bascones, E. The nature of correlations in the insulating states of twisted bilayer graphene. *Journal of Physics Communications* **3**, 035024 (2019).
22. Keimer, B. & Moore, J. E. The physics of quantum materials. *Nat. Phys.* **13**, 1045 (2017).
23. Si, Q., Yu, R. & Abrahams, E. High-temperature superconductivity in iron pnictides and chalcogenides. *Nat. Rev. Mater.* **1**, 16017 (2016).
24. Zhu, G.-Y., Xiang, T. & Zhang, G.-M. Inter-valley spiral order in the mott insulating state of a heterostructure of trilayer graphene-boron nitride. *Science Bulletin* **63**, 1087–1091 (2018).
25. Zhang, Y.-H. & Senthil, T. Bridging hubbard model physics and quantum hall physics in trilayer graphene/ h – BN moiré superlattice. *Phys. Rev. B* **99**, 205150 (2019).
26. Po, H. C., Zou, L., Vishwanath, A. & Senthil, T. Origin of mott insulating behavior and superconductivity in twisted bilayer graphene. *Phys. Rev. X* **8**, 031089 (2018).
27. Yuan, N. F. Q. & Fu, L. Model for the metal-insulator transition in graphene superlattices and beyond. *Phys. Rev. B* **98**, 045103 (2018).
28. Hu, W.-J. *et al.* Nematic and antiferromagnetic quantum criticality in a multi-orbital hubbard model for iron pnictides. *arXiv preprint arXiv:1903.12625* (2019).
29. Yu, R. & Si, Q. $u(1)$ slave-spin theory and its application to mott transition in a multiorbital model for iron pnictides. *Phys. Rev. B* **86**, 085104 (2012).
30. Hussey, N. E., Takenaka, K. & Takagi, H. Universality of the Mott–Ioffe–Regel limit in metals. *Philos. Mag.* **84**, 2847 (2004).

31. Tang, Y. *et al.* Simulation of Hubbard model physics in WSe₂/WS₂ moiré superlattices. *Nature* **579**, 353–358 (2020).
32. Regan, E. C. *et al.* Mott and generalized Wigner crystal states in WSe₂/WS₂ moiré superlattices. *Nature* **579**, 359–363 (2020).
33. Wang, L. *et al.* Correlated electronic phases in twisted bilayer transition metal dichalcogenides. *Nature Materials* 1–6 (2020).
34. Koshino, M. & McCann, E. Trigonal warping and berry’s phase $n\pi$ in abc-stacked multilayer graphene. *Phys. Rev. B* **80**, 165409 (2009).
35. Zhang, F., Sahu, B., Min, H. & MacDonald, A. H. Band structure of *abc*-stacked graphene trilayers. *Phys. Rev. B* **82**, 035409 (2010).
36. Kumar, A. *et al.* Integer quantum hall effect in trilayer graphene. *Phys. Rev. Lett.* **107**, 126806 (2011).
37. Zhang, Y.-H., Mao, D., Cao, Y., Jarillo-Herrero, P. & Senthil, T. Nearly flat chern bands in moiré superlattices. *Phys. Rev. B* **99**, 075127 (2019).
38. Capello, M., Becca, F., Fabrizio, M., Sorella, S. & Tosatti, E. Variational description of mott insulators. *Phys. Rev. Lett.* **94**, 026406 (2005).
39. McCann, E. & Koshino, M. The electronic properties of bilayer graphene. *Reports on Progress in Physics* **76**, 056503 (2013).
40. Tocchio, L. F., Becca, F. & Sorella, S. Hidden mott transition and large- u superconductivity in the two-dimensional hubbard model. *Phys. Rev. B* **94**, 195126 (2016).
41. De Franco, C., Tocchio, L. F. & Becca, F. Metal-insulator transitions, superconductivity, and magnetism in the two-band hubbard model. *Phys. Rev. B* **98**, 075117 (2018).

Acknowledgments

We acknowledge useful discussions with D. P. Arovas, F. Becca, D. Goldhaber-Gordon, W.-J. Hu, A. H. MacDonald, A. Pasupathy, T. Senthil and J. Shan. This work has been supported in part by the the U.S. DOE, BES under Award # DE-SC0018197 and the Robert A. Welch Foundation Grant No. C-1411. The majority of the computational calculations have been performed on the Shared University Grid at Rice funded by NSF under Grant EIA-0216467, a partnership between Rice University, Sun Microsystems, and Sigma Solutions, Inc., the Big-Data Private-Cloud Research Cyberinfrastructure MRI-award funded by NSF under Grant No. CNS-1338099 and by Rice University, the Extreme Science and Engineering Discovery Environment (XSEDE) by NSF

under Grant No. DMR160057.

Author contributions

The first two authors contributed equally to this work. All authors contributed to the research of the work and the writing of the paper.

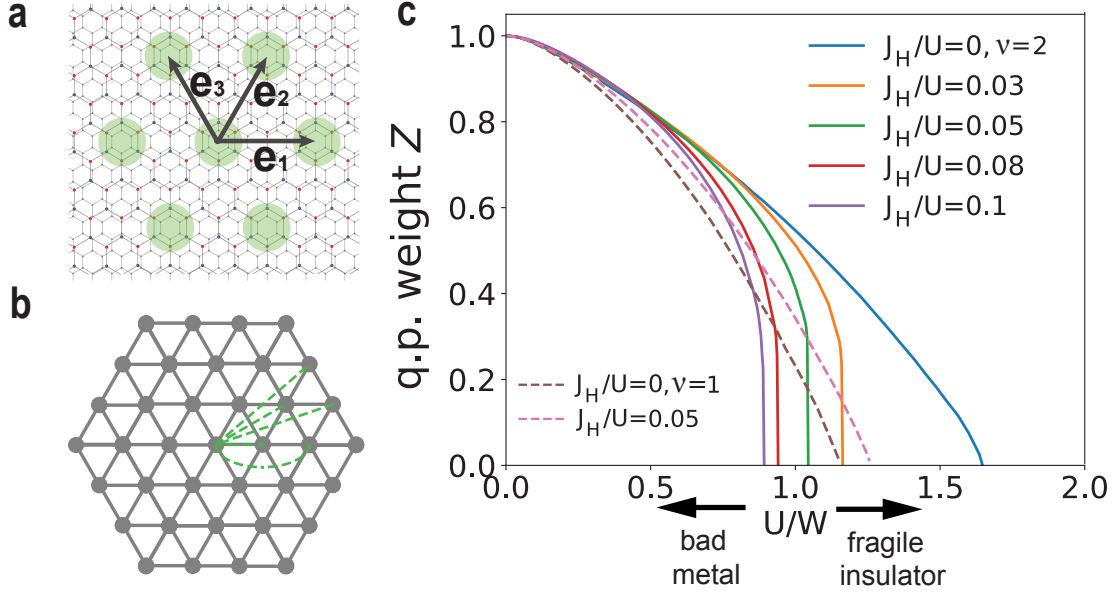


FIG. 1: A graphene moiré system and the development of fragile insulator and bad metal. **a**, Illustration of the moiré superlattice, where \mathbf{e}_1 , \mathbf{e}_2 , \mathbf{e}_3 denote the superlattice basis vectors. The triangular lattice, marked by the green regions, results from a difference in the lattice constants between TGL and hBN. **b**, The bonds (dashed lines) for the hopping parameters, $t_1 - t_5$, of the effective tight binding model. Through the C_6 and M_y transformations, they specify the parameters for other bonds in the moiré superlattice. **c**, The quasiparticle (q.p.) weight Z as a function of U/W . The results show the strong influence of the Hund's coupling J_H on the metal-insulator transition. For $J_H/U = 0, 0.03, 0.05, 0.08, 0.1$ at the half filling ($\nu = 2$) of the moiré bands, the Mott transition thresholds are $U_c/W = 1.65, 1.16, 1.04, 0.94, 0.89$, respectively. For $J_H/U = 0, 0.05$ at the quarter filling ($\nu = 1$), they are $U_c/W = 1.15, 1.26$, respectively.

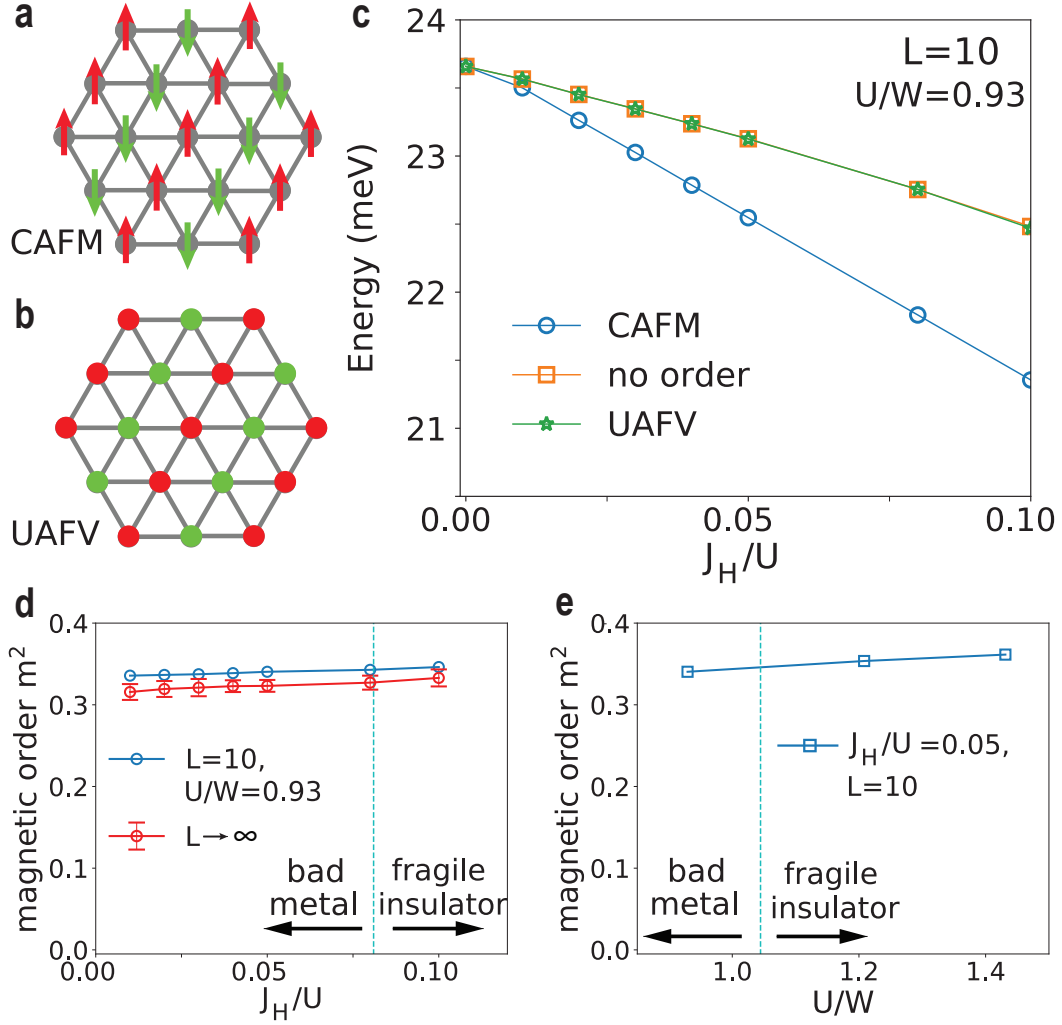


FIG. 2: Ground state at half filling. **a**, Illustration of the collinear antiferromagnetic order (CAFM). The red and green spins are opposite of each other. **b**, That of the uniaxial antiferrovalley order (UAFV). The red (green) sites represent $(n_+ - n_-) > (<) 0$. **c**, The ground state energy of the different states as a function of J_H/U for a fixed U/W . The VMC calculation is performed on a $L \times L$ geometry (Supplementary Information, Fig. S2). **d**, The magnetic order parameter (m^2) as a function of the Hund's coupling J_H/U for a fixed Hubbard interaction $U/W = 0.93$, at $L = 10$ and estimated from a finite size scaling ($L \rightarrow \infty$, see Supplementary Information, Fig.,S4). The magnetic order persists for J_H/U as small as 0.01. **e**, The magnetic order parameter (m^2) as a function of U/W for fixed $J_H/U = 0.05$.

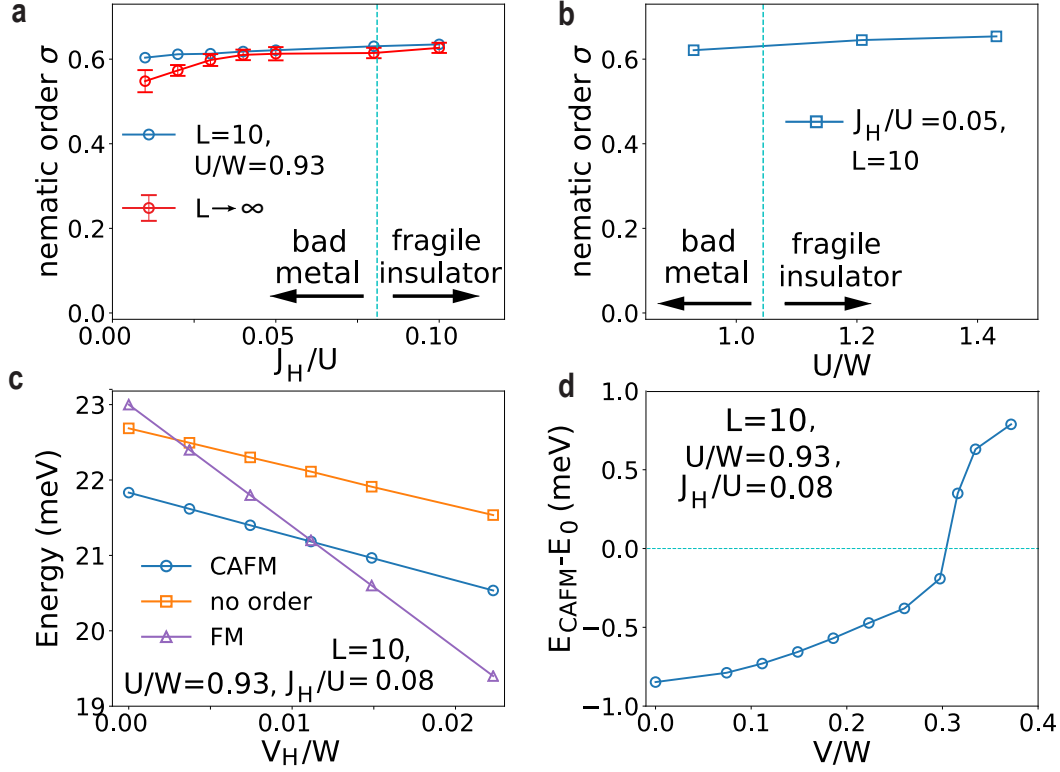


FIG. 3: **Nematic order and its stability.** **a**, The nematic order parameter (σ) as a function of the Hund's coupling J_H/U for fixed Hubbard interaction $U/W = 0.93$, calculated at $L = 10$ and estimated for the limit $L \rightarrow \infty$ based on a finite size scaling procedure (see Supplementary Information, Fig. S4). **b**, The nematic order parameter (σ) as a function of U/W for fixed $J_H/U = 0.05$. **c**, The energy of the CAFM, non-ordered and ferromagnetic (FM) states vs. the nearest-neighbor exchange interaction V_H/W at $J_H/U = 0.08$ and $U/W = 0.93$. The threshold value for the FM state with a lower energy is $V_H^1/W \approx 0.011$. **d**, The difference in the ground state energy between CAFM and the non-ordered state vs. the nearest-neighbor repulsion V/W at $J_H/U = 0.08$ and $U/W = 0.93$. The crossing interaction strength is $V^1/W \approx 0.31$.

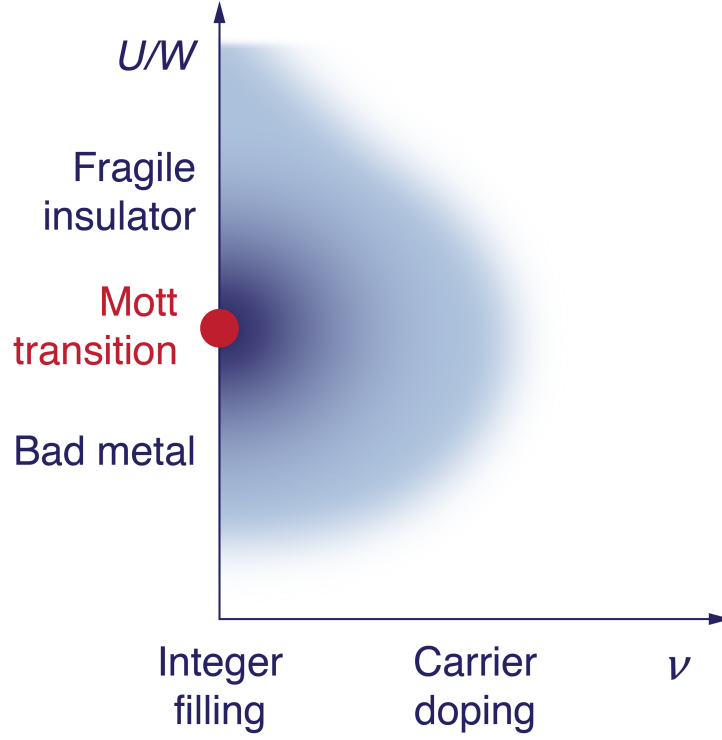


FIG. 4: **Schematic phase diagram involving fragile insulator and bad metal.** At an integer filling, fragile insulator and bad metal are on two sides of an electron localization transition (red point, a Mott transition) as a function of the interaction U/W . Both control the fluctuations in the magnetic and valley channels, thereby anchoring the physics in the regime where the carrier concentration (ν) is away from the integer filling; this is marked by the shaded blue region.

Methods

The multiorbital Hubbard model The lowest energy levels of the original ABC stacked graphene (see Supplementary Information, Fig. S1) can be modeled as a two-band effective model with cubic band touching at K_+ and K_- momenta of the original BZ^{34–36}. The perpendicular voltage bias generates an energy difference, Δ_V , between the top and bottom layers. The hBN layer provides a superlattice potential (Fig. 1a), with components at the reciprocal lattice vectors of the moiré lattice, which is the origin of the moiré bands. The combination of these terms lead to a two-orbital Hubbard model defined on a triangular lattice (*cf.* Fig. 1b), as given in Ref. 25:

$$\begin{aligned}
 H &= H_0 + H_U + H_V, \\
 H_0 &= \sum_{\mathbf{k}, \sigma \alpha} \epsilon_{\mathbf{k}, \alpha} c_{\mathbf{k}, \alpha \sigma}^\dagger c_{\mathbf{k}, \alpha \sigma}, \\
 H_U &= \sum_i \frac{U}{2} n_i^2 - J_H \sum_i \left(\frac{1}{4} n_{+,i} n_{-,i} + \mathbf{S}_{+,i} \cdot \mathbf{S}_{-,i} \right), \\
 H_V &= \sum_{\langle i, j \rangle} \left[V n_i n_j - \sum_{\alpha_1 \alpha_2 \sigma_1 \sigma_2} V_H c_{i, \alpha_1 \sigma_1}^\dagger c_{i, \alpha_2 \sigma_2} c_{j, \alpha_2 \sigma_2}^\dagger c_{j, \alpha_1 \sigma_1} \right].
 \end{aligned} \tag{3}$$

Here, $c_{\mathbf{k}, \alpha \sigma}^\dagger$ creates an electron of wavevector \mathbf{k} , valley $\alpha = +$ or $-$ and spin σ , and H_0 describes the kinetic part, with hopping parameters up to the 5th nearest neighbors (*cf.* Fig. 1b). The time reversal symmetry dictates $\epsilon_{\mathbf{k}, +} = \epsilon_{-\mathbf{k}, -}$. The complex hopping terms break the spin-valley U(4) symmetry down to $U(2)_+ \times U(2)_-$ (Refs. 25,37). Additionally, H_U contains the onsite interactions: the Hubbard interaction U preserves the spin-valley U(4) symmetry, while the inter-valley Hund's coupling J_H breaks this symmetry down to $U(1)_c \times U(1)_v \times SU(2)_s$. The density and spin operators are defined as $n_{\alpha, i} = \sum_\sigma c_{i, \alpha \sigma}^\dagger c_{i, \alpha \sigma}$, $n_i = \sum_\alpha n_{\alpha, i}$, and $\mathbf{S}_{\alpha, i} = \frac{1}{2} \sum_{\sigma \sigma'} c_{i, \alpha \sigma}^\dagger \boldsymbol{\tau}_{\sigma \sigma'} c_{i, \alpha \sigma'}$ respectively, with $\boldsymbol{\tau}$ being the Pauli matrices. Finally, H_V contains the nearest-neighbor interactions: V is for density-density, and V_H for spin-valley exchange.

Variational Monte Carlo method We follow the VMC approach of Ref. 28, which incorporated a spin Jastrow factor in the Jastrow-Slater wavefunction³⁸ (in addition to the usual density Jastrow factor) to treat the correlation effect of the Hund's coupling non-perturbatively. The $L \times L$ geometry of our simulation is illustrated in the Supplementary Information, Fig. S2.

U(1) slave-spin method In the U(1) slave-spin method²⁹, the electron creation operator is expressed in terms of an xy spin operator $S_{i, \alpha \sigma}^+$, which represents the charge degree of freedom, and a fermionic 'spinon' operator $f_{i, \alpha \sigma}$: $c_{i, \alpha \sigma}^\dagger = S_{i, \alpha \sigma}^+ f_{i, \alpha \sigma}^\dagger$. This is accompanied by a local constraint:

$S_{i,\alpha\sigma}^z + 1/2 = f_{i,\alpha\sigma}^\dagger f_{i,\alpha\sigma}$. A set of self-consistent equations provide a saddle-point description, which results in the quasi-particle weight $Z_{\alpha\sigma} = |\langle P S_{\alpha\sigma}^+ P \rangle|^2$, where P is a projection operator to enforce the local constraint.

Nematic order The model, defined on the triangular lattice, has a C_6 rotational symmetry. However, weak terms that have been neglected in the Hamiltonian would reduce the symmetry to C_3 . We have therefore constructed the different possible channels of nematic order from the irreducible representations of both the D_6 and D_3 point groups. The result is shown in Table I. The nematic order that is important for the present work is in the E_2/E channel, in the two classification schemes respectively.

In TBG systems, the symmetry group is D_6 or D_3 depending on the twisting center, and the majority of the spectral weights stays on an effective triangular moiré superlattice. The same symmetry classification of the nematic orders applies to the TBG system.

Irr. Rep. (D_6)	Irr. Rep. (D_3)	Nematic order
B_1	A_1	$\frac{1}{\sqrt{6}} \sum (-1)^r B_r$
E_1	E	$\frac{1}{\sqrt{6}} \sum e^{i\frac{r\pi}{3}} B_r, \frac{1}{\sqrt{6}} \sum e^{i\frac{5r\pi}{3}} B_r$
E_2	E	$\frac{1}{\sqrt{6}} \sum e^{i\frac{2r\pi}{3}} B_r, \frac{1}{\sqrt{6}} \sum e^{i\frac{4r\pi}{3}} B_r$

TABLE I: The classification of the nematic order. Here, the nearest-neighbor-bond operators are $B_r = \frac{1}{N} \sum_i \mathbf{S}_i \cdot \mathbf{S}_{i+e_r}$, where $\{e_r\}_{r=1,\dots,6}$ denote the set of six nearest neighbors, with e_1, e_2, e_3 shown in Fig. 2b, and $e_4, e_5, e_6 = -e_1, -e_2, -e_3$.

Supplementary Information

Bandstructure and Fermi surface

We outline the bandstructure, both over an extended energy range and for the bands retained in the model, and the Fermi surface^{14,25,37}. We will use the notation of Ref. 25 for the most part. If one firstly ignores the hBN layer and focuses on the ABC stacked trilayer graphene (*cf.* Fig. S1), the bare hopping parameters are known in the literature³⁹, and there is an energy difference Δ_V between the top and bottom layers. There is cubic band touching at each of the two momenta, K_{lbz} and K'_{lbz} of the original (large) Brillouin zone, which are labeled as valley $+$ and $-$. One can integrate out the higher energy states to construct an effective Hamiltonian for the electron states associated with the top (t) and bottom (b) layers. The low energy behavior in each valley is described by a two band model, counting the contributions from the A sublattice of the top layer and B sublattice from the bottom layer³⁴. The aligned hBN substrate creates a potential for the adjacent graphene layer. This potential comprises components at the morié superlattice Bravais vectors for each of the two valleys. Diagonalizing this Hamiltonian numerically up to the 5th $q_M = \frac{4\pi}{3a_M}$, where $a_M \approx \frac{a_1 a_2}{a_1 - a_2} \approx 58a$ with $a_{1,2}$ being the lattice constants of the TLG and hBN, yields the band dispersion in the extended energy range (Fig. S3b,c). The two sets of morié bands are separated by a gap, as opposed to be gapless with Dirac points in the TBG case.

For different signs of Δ_V , the Fermi energy crosses two different sets of the morié bands: those for $\Delta_V > 0$ have nonzero Chern numbers, while those for $\Delta_V < 0$ do not. In the latter case, the effective Hamiltonian is a two-band Hubbard model defined on the triangular lattice illustrated in Fig. 1a, as presented in Eq. (3) (Ref. 25). The kinetic part has the following form:

$$H_0 = - \sum_{ij} t_{ij} c_{+\sigma}^\dagger c_{+\sigma} - \sum_{ij} t_{ij}^* c_{-\sigma}^\dagger c_{-\sigma} + h.c., \quad (S1)$$

where \pm is the valley index and $\sigma = \uparrow, \downarrow$ is the spin index. The tight-binding parameters, as illustrated in Fig. 1b of the main text; for the case of $\Delta_V = -20$ meV are $t_1 = 1.583e^{i0.169\pi}$ meV, $t_2 = -1.108$ meV, $t_3 = 0.732e^{-i0.653\pi}$ meV and $t_4 = t_5^* = 0.323e^{-i0.069\pi}$ meV (Ref. 25). Those for the other symmetry-related bonds are generated by the C_6 rotation and M_y reflection. This morié band structure is shown in Fig. S3a, with a bandwidth $W = 26.9$ meV. The path along which the band structure is shown is given in Fig. S3d. The Fermi surfaces of each band in the half-filling cases are presented in Fig. S3d,e,f.

Finite size scaling for the order parameters

The magnetic and nematic orders with $L = 8, 10, 12, 14, 16$ are shown in Fig. S4a,b. To extrapolate to the thermal dynamical limit, finite size scaling over the system size is performed and is illustrated in Fig. S4c,d. Polynomial fittings, with the exponent up to 2, are performed. The error bars are estimated as the standard deviation between the simulated results and the estimated values of the fitted curves.

Details of the Variational Monte Carlo method

The VMC approach is adapted from that of Ref. 28, which considered a square lattice. Here, the model is defined on a triangular lattice. As in Ref. 28, a spin Jastrow factor is used, in addition to the usual density Jastrow factor, to treat the correlation effect of the Hund's coupling. The uncorrelated state $|\Phi_0\rangle$ is specified by the following auxiliary (quadratic) Hamiltonian^{40,41}:

$$\begin{aligned} \mathcal{H}_{\text{aux}} = & - \sum_{\alpha=\pm, i, j, \sigma} (1 + \delta\tilde{\alpha}_{ij}) t_{ij} \left(c_{\alpha, i, \sigma}^\dagger c_{\alpha, j, \sigma} + h.c. \right) - \sum_{\sigma, i, j} \delta\tilde{t}_{ij} \left(c_{+, i, \sigma}^\dagger c_{-, j, \sigma} + h.c. \right) \\ & + \sum_{\alpha, i, \sigma} \tilde{\mu}_\alpha c_{\alpha, i, \sigma}^\dagger c_{\alpha, i, \sigma} + \sum_{\alpha, i} e^{i\mathbf{Q}_{mag} \cdot \mathbf{R}_i} \Delta_\alpha^{AFM} \left(c_{\alpha, i, \uparrow}^\dagger c_{\alpha, i, \downarrow} + c_{\alpha, i, \downarrow}^\dagger c_{\alpha, i, \uparrow} \right) \\ & + \sum_{i, \sigma} e^{i\mathbf{Q}_{orb} \cdot \mathbf{R}_i} \Delta^{AFV} \left(c_{+, i, \sigma}^\dagger c_{+, i, \sigma} - c_{-, i, \sigma}^\dagger c_{-, i, \sigma} \right) \end{aligned} \quad (\text{S2})$$

where $\delta\tilde{\alpha}_{ij}$, $\delta\tilde{t}_{ij}$, $\tilde{\mu}_\alpha$, and Δ_α^{AFM} , Δ^{AFV} are variational parameters. The first two terms came from the renormalization of the hopping. For the intra-valley hopping, we fix the phase to be the same as for the non-interacting limit, while introducing the amplitude scaling variables $(1 + \delta\tilde{\alpha}_{ij})$. The presence of $\Delta_\alpha^{AFM} (\Delta^{AFV}) \neq 0$, implies magnetic (valley) order. By choosing \mathbf{Q}_{mag} (\mathbf{Q}_v) to be \mathbf{K} ($\frac{4}{3}\pi, 0$) or \mathbf{M} ($\pi, \frac{1}{\sqrt{3}}\pi$), we can have either three sublattice (120°)-like or two sublattice magnetic (valley) orders. The geometry is shown in S2, with the periodic boundary condition (PBC) for both directions. Each direction has a linear dimension L ; the total number of sites is $N = L \times L$.

Hartree-Fock calculation

We perform Hartree-Fock calculations to study the phase diagram and stability of the CAFM phase in the presence of the nearest-neighbor interaction terms of H_V . Here, except for the FM, CAFM, UAFV and non-ordered phases that have been studied by the VMC method, we also include the charge-ordered phase with wavevector \mathbf{K} (CO-K), which is a three-sublattice order with the particle numbers being different in the different sublattices. This type of order can be favored when the nearest-neighbor repulsion V is sufficiently large. Finally, with a sizable $t_2^2/|t_1|^2 \approx 0.49$, we can expect that the CAFM phase is energetically favored compared with any three-sublattice AFM. Our calculation of the AFM-K phase indicates that this is indeed the case.

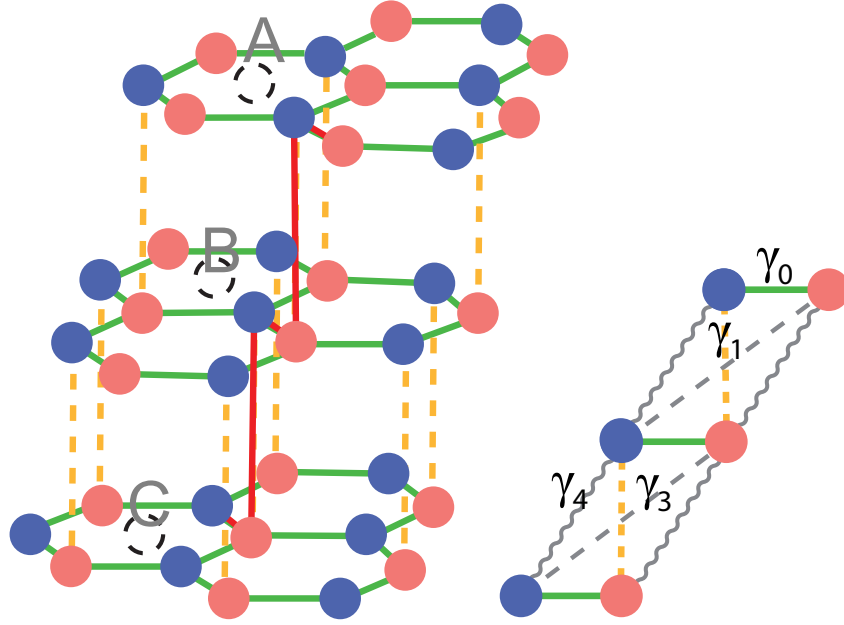


FIG. S1: **Illustration of the ABC stacked trilayer graphene.** The γ 's label the tight-binding parameters that are used to construct the bandstructure³⁹.

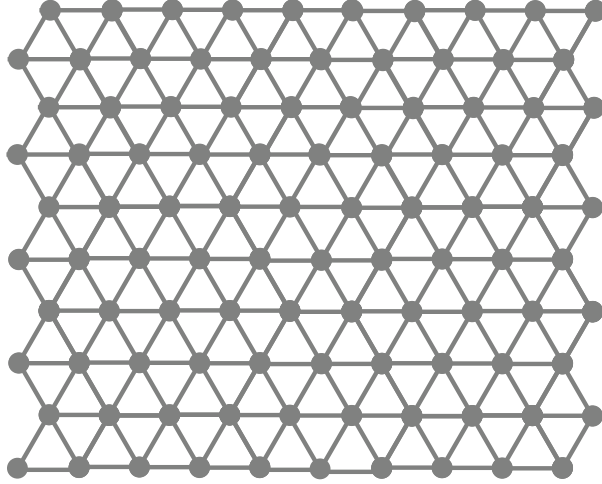


FIG. S2: The real space structure of the morié superlattice for the VMC calculation.

Illustrated here is the $L \times L$ case with $L = 10$. The periodic boundary condition is implemented for each direction.

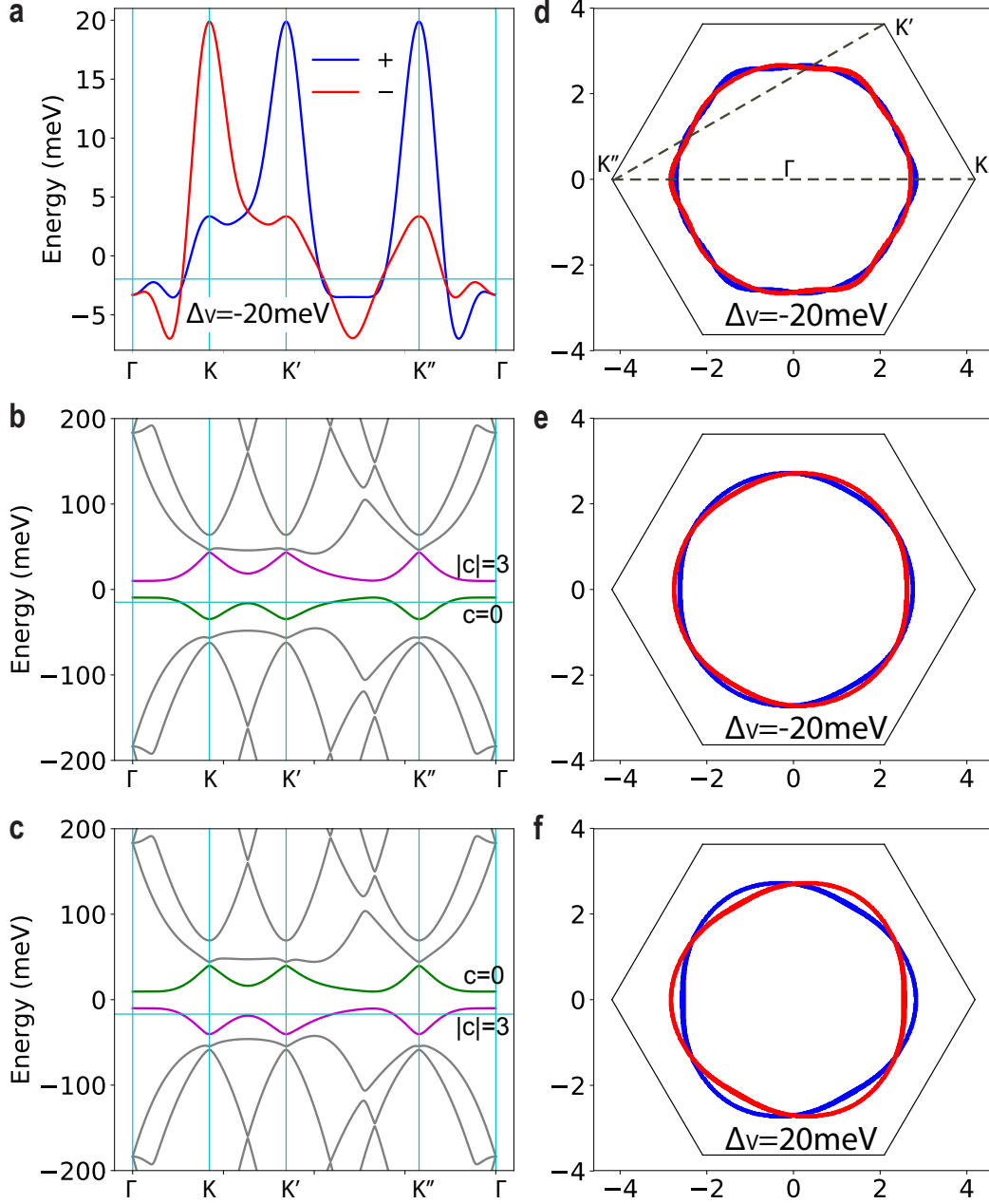


FIG. S3: Bandstructure and the Fermi surface. **a**, The band structure of the two-orbital Hubbard model, including the bands for both valleys. The bandwidth is $W \approx 26.9$ meV. The horizontal cyan line represents the Fermi energy for half filling. **b**, The band structure of the continuum model with the perpendicular bias energy for the $+$ valley. The Fermi energy crosses the band with the Chern number $c = 0$. **c**, The counterpart of **b** for $\Delta_V = 20$ meV. The Fermi energy crosses the bands with nonzero c . **d**, The Fermi surface at half-filling for the tight binding model, for the case of $\Delta_V = -20$ meV. **e**, The Fermi surface for the filling as in **d**, but calculated from the continuum model with $\Delta_V = -20$ meV. **f**, The counterpart of **e** for $\Delta_V = 20$ meV.

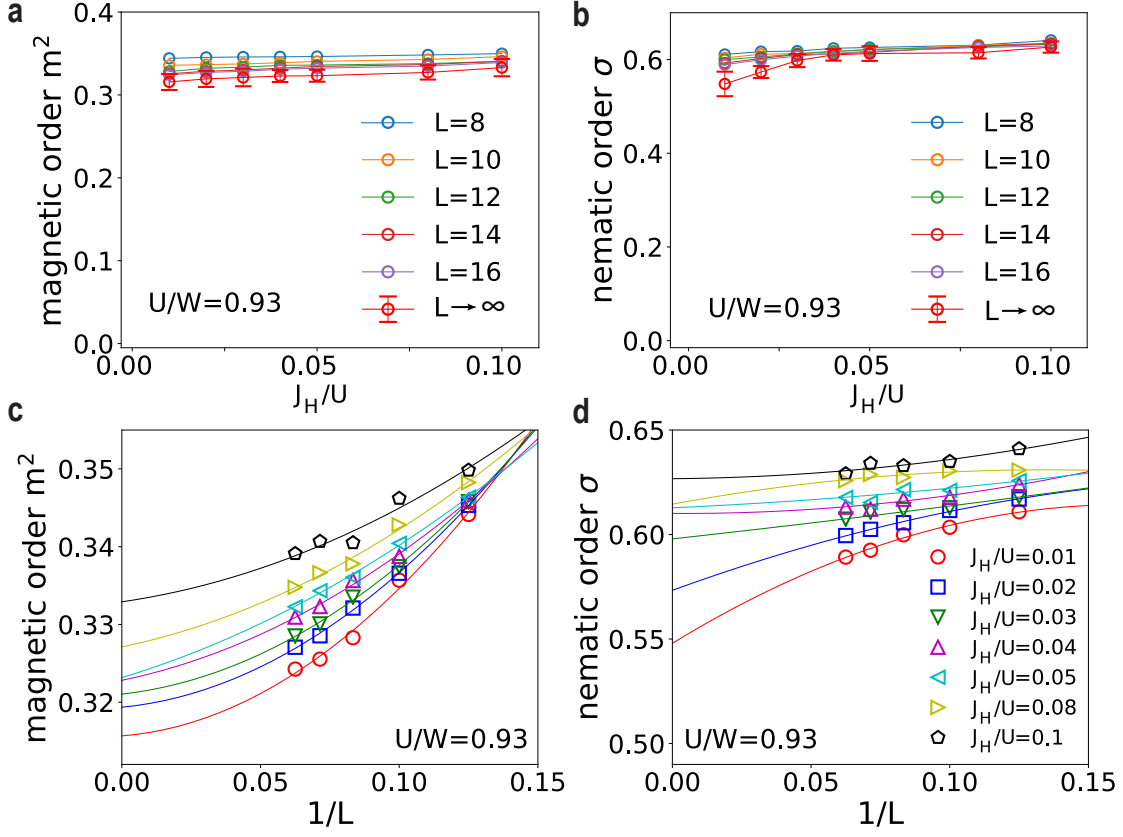


FIG. S4: Size dependence and finite size scaling of the magnetic and nematic order parameters. **a**, Magnetic order parameter m^2 as a function of J_H/U for fixed U/W , at different sizes $L = 8, 10, 12, 14, 16$ and in the limit $L \rightarrow \infty$ based on finite size scaling. **b**, Counterpart of **a** for the nematic order parameter σ . **c,d**, Finite size scaling of the magnetic and nematic order parameters, for the different values of J_H/U with fixed U/W .

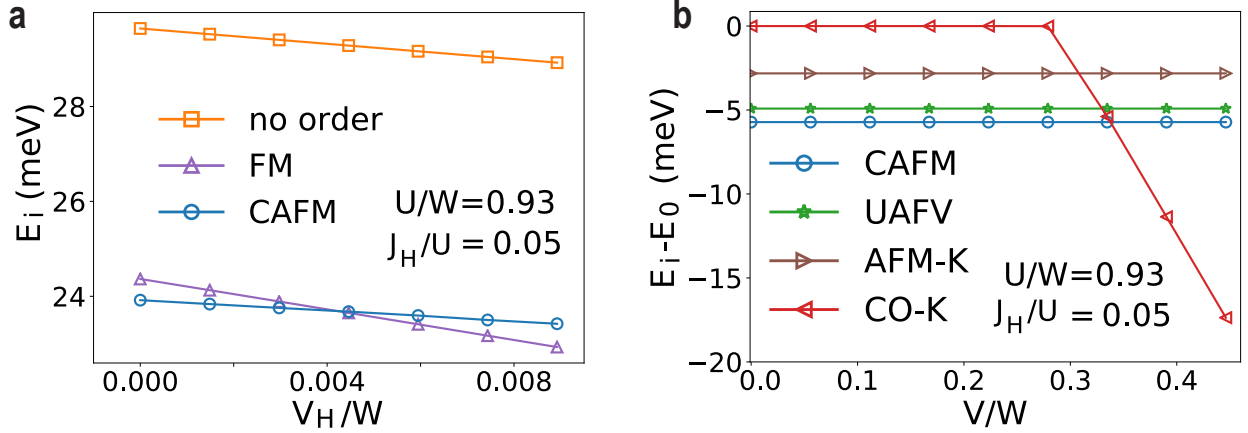


FIG. S5: **Result of the self-consistent Hartree-Fock calculation.** **a**, The ground state energies of the various symmetry-broken phases and the paramagnetic phase (no order) versus the nearest-neighbor exchange interaction V_H/W with fixed $U/W = 0.93$ and $J_H/U = 0.05$. Here i includes no order, ferromagnetic (FM) and collinear antiferromagnetic order (CAFM). **b**, The difference between the ground state energy of a broken symmetry phase i and that of the paramagnetic phase 0 versus the nearest-neighbor density-density interaction V/W . Here, i includes CAFM, the uniaxial antiferrovalley (UAFV) order, collinear antiferromagnetic order with wavevector \mathbf{K} (AFM-K) and charge order with wavevector \mathbf{K} (CO-K).